Appl Phys B (2012) 108:615–621
DOI 10.1007/s00340-012-5007-8

**Applied Physics B**
**Lasers and Optics**

# Comparison of one- and three-dimensional computational fluid dynamics models of the supersonic chemical oxygen–iodine laser

**I. Brami-Rosilio · B.D. Barmashenko · S. Rosenwaks**

Received: 2 January 2012 / Revised version: 21 February 2012 / Published online: 21 April 2012


**Abstract** A simple one-dimensional (1D) computational fluid dynamics (CFD) model of the chemical oxygen iodine laser (COIL) with supersonic mixing is compared with three-dimensional (3D) CFD models and with experimental measurements of the COIL parameters. Dependence of the gain, iodine dissociation fraction and temperature at the resonator optical axis and of the output lasing power on the iodine flow rate predicted by the 1D model is in good agreement with that found using 3D models and experimental results. Hence the 1D model can be used instead of much more complicated 3D models for estimates of the working parameters of supersonic COILs.

## 1 Introduction

The chemical oxygen-iodine laser (COIL) [1] operates on the electronic transition of the I atom $I(^2P_{1/2}) \rightarrow I(^2P_{3/2})$ and emits at 1315 nm. The complex kinetic, mixing and laser oscillation processes that take place in the reactive medium of the supersonic COIL can be described using either one-dimensional (1D) or three-dimensional (3D) computational fluid dynamics (CFD) models. 3D CFD models of the COIL [2–9] predict detailed pattern of the flow field in the laser and, in particular, the shape of the jets injected into the cross flow, non-uniform distribution of the gain and temperature across the flow, shocks, flow unsteadiness and turbulence. Both the gain and the power for different types of COIL calculated over the entire range of their parameters using 3D CFD models are in good agreement with the measured values [7–9]. 1D CFD models [10–15], developed mainly in the 1990s, reproduce most of the essential features of the chemical kinetics, hydrodynamics and lasing in the active medium of the COIL, though they give distributions of the small signal gain and temperature only in the flow direction. The major advantage of 1D modeling is reducing the computation time: while for the 1D model it requires about 10 seconds to get results for a single set of conditions, for the 3D model it requires four orders of magnitude longer to carry out the same computation.

In the present paper a simple 1D CFD model of a supersonic COIL with iodine injection in the supersonic section of the nozzle is developed. Dependence of the gain, temperature and $I_2$ dissociation fraction at the optical axis and of the lasing power on the iodine flow rate is found and compared with that calculated using the 3D CFD model reported in [8] and [9] and with the experimental results presented in the same references.

## 2 Outline of the model

The present model is based on the 1D model of a COIL with transonic injection of iodine developed in [15]; however, there are several important differences between the models which will be listed below. We therefore briefly outline here the main assumptions of the model. The model considers a typical configuration of a low pressure supersonic COIL where the primary $O_2(a)/O_2(X)$ flow (where $O_2(a) \equiv O_2(a^1\Delta_g)$ and $O_2(X) \equiv O_2(X^3\Sigma_g^-)$) is expanded supersonically through a slit supersonic nozzle with injection of the secondary $N_2/I_2$ flow at a 45° angle to the primary flow in the diverging section of the nozzle through a row of 25, 1.4-mm diameter holes in the upper and lower

I. Brami-Rosilio · B.D. Barmashenko (✉) · S. Rosenwaks
Department of Physics, Ben-Gurion University of the Negev, Beer-Sheva 84105, Israel
e-mail: barmash@bgu.ac.il
Fax: +972-8-6472904

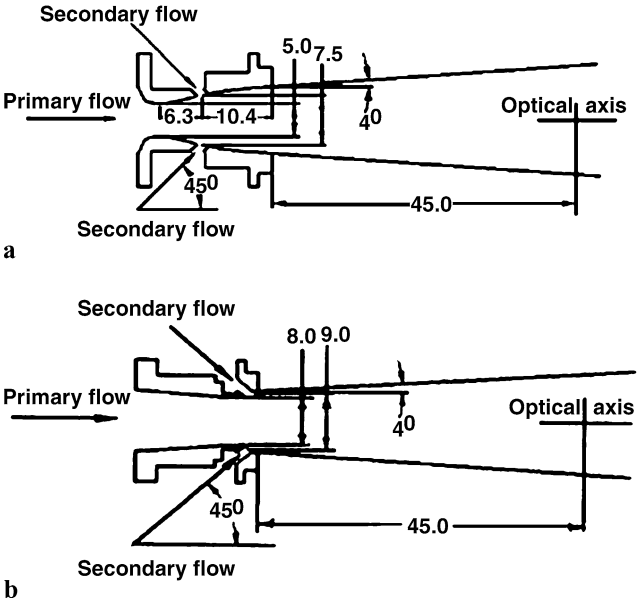


**Fig. 1** Schematics of the slit nozzles used in the supersonic COIL. All measures are in millimeters; (**a**) profiled 5-mm throat height nozzle [8]; (**b**) non-profiled 8-mm throat height nozzle [9]

nozzle wall. Two different nozzles are studied: a profiled 5-mm throat height nozzle and non-profiled 8-mm throat height nozzle shown in Fig. 1(a) and (b), respectively. The first nozzle was used for measurements of the gain, temperature and $I_2$ dissociation fraction [6], whereas the second for power measurements [16]. Comparison between the calculated and measured gain and power could not be done for the same nozzle because extensive experimental data for the gain and the power was available for different nozzles. The laser section of the COIL starts at the nozzle exit plane (flow cross section of $5 \times 1$ cm$^2$) from where the floor and the ceiling of the flow duct diverge at an angle of 8°. The optical axis of the resonator is transverse to the flow direction and located 45 mm downstream of the nozzle block exit plane. For power computations the mirror length in the flow direction was 3.6 cm and its vertical dimension ∼1.7 cm: the mirror output aperture was formed by the diverging ceiling and floor of the flow duct and the edges of the holes cut in the side walls of the duct and connecting the laser active volume with the mirror shrouds.

As follows from the 3D distributions of the Mach number obtained in [6] and [7], the $N_2/I_2$ jets injected into the primary flow bend and block the primary flow, resulting in formation of an aerodynamic throat with a height smaller than the geometrical nozzle height, where the cross section of the primary flow is minimal. Unlike the 1D case treated in [15] (transonic mixing), the aerodynamic throat for the 3D case is located downstream of the injection holes (and hence downstream of the geometrical nozzle throat) at a distance close to the half-height of the nozzle at the injection location. The bending for the 3D case is accompanied by fast mixing and chemical reactions between the primary and secondary flows resulting in $I_2$ dissociation into atoms and excitation of I [$\equiv$I($^2P_{3/2}$)] atom into the upper laser level I$^*$ [$\equiv$I($^2P_{1/2}$)] by energy transfer from $O_2(a)$:

$$O_2(a) + \mathrm{I} \quad \leftrightarrow \quad O_2(X) + \mathrm{I}^*. \tag{1}$$

For simplicity it was assumed for the present 1D model (mixing in the supersonic section of the nozzle) that after the bending of the jets is completed the parallel primary and secondary streams are instantaneously mixed at the aerodynamic throat and there is no any mixing computed upstream of the throat. We assumed that just as in the aforementioned 3D case, the aerodynamic throat is located downstream of the injection holes at a distance equal to the half-height of the nozzle at the injection location. 1D computations show that the height of the aerodynamic nozzle is ∼60 % of the geometrical nozzle height. Then the mixed stream undergoes supersonic expansion accompanied by chemical reactions. This process continues towards the optical resonator.

Just as in [15], the model is divided into two main parts. The first part calculates the initial conditions in the mixed stream at the critical cross section of the flow. The primary stream parameters before mixing with the secondary stream are equal to the critical flow parameters for Mach number equal to unity. Parameters of the secondary stream (temperature, velocity and cross section), which as mentioned above is parallel to the primary one, before the mixing are found from the given secondary flow rates, $nI_2$ and $nN_2$, and the stagnation pressure and temperature of the secondary flow assuming equal static pressures in the primary and secondary streams. The computation is performed for isentropic approximation for both flows; to take into account non-isentropic effects of the shock waves and viscosity in the secondary flow, its stagnation pressure is corrected by the loss factor $P0_{L1} = 0.75$ [15]. Flow parameters of the mixed stream are found from mass, momentum and energy conservation conditions assuming that the static pressure does not change during the mixing process. However, unlike [15], the efficiency of the instantaneous mixing is assumed to be equal to unity which means that the entire primary stream is mixed with the secondary flow and instead of the two streams (primary and mixed) considered in [15] only one mixed stream is formed. This assumption is in line with the results of [17] where the mixing efficiency for iodine injection at the supersonic section of the nozzle (∼0.85) was found to be much larger than for transonic injection (∼0.5). The reason for high mixing efficiency for the supersonic injection is that the secondary $N_2$ flow rate is much larger than for transonic injection. As a result, ejector COIL operation mode [19] takes place. As shown in [19], for this operation mode, large values of the secondary $N_2$ flow result in large velocity gradients in the transverse direction, and hence in fast convective mass transfer in the supersonic section of the COIL.

In the second part of the model the mass flow rates $\omega(Z)$ of species $Z$, the temperature $T$ and the velocity $U$ are calculated by solving the conservation differential equations, considering the supersonic expansion and the chemical reactions occurring in the stream. These equations are presented in the Appendix. The final conditions after the instantaneous mixing, as calculated in the first part of the model, serve as the initial conditions for the differential equations. A spatial dependence of the pressure along the flow was assumed and found from the linear interpolation of the pressures measured at three points in the supersonic section of the flow and the critical pressure. In order to take into account non-isentropic effects during the expansion in the slit nozzle (shock waves and boundary layers), we assumed that the stagnation pressure in the stream drops in the diverging section of the nozzle and the loss factor $P0_{L2}$ is 0.75 [15].

The above-mentioned differential equations are solved numerically using the Matlab program. Computation time for one run was usually less than 10 seconds on a conventional PC (Intel(R) Core(TM)2 CPU, 1.86-GHz, 1-GB of RAM). In addition to other flow parameters, the gain $g$ and the iodine dissociation fraction $F$ were calculated at the optical axis of the resonator for the runs without lasing; they are given by [15]:

$$g = \frac{7}{12}\sigma\left(\left[\mathrm{I}^*\right] - 0.5[\mathrm{I}]\right), \tag{2}$$

and

$$F = 1 - \omega(\mathrm{I}_2)/\omega_0(\mathrm{I}_2), \tag{3}$$

where $\sigma = 1.29 \times 10^{-17}(300/T)^{1/2}$ cm$^2$ is the stimulated emission cross section and $\omega_0(\mathrm{I}_2)$ is the initial mass flow rate of $\mathrm{I}_2$ before injection. It was assumed that $F = 0$ upstream of the aerodynamic throat. For some runs the total output laser power was calculated as explained below.

The model uses a set of chemical reactions based on the Heidner–Lilenfeld–Azyazov–Heaven–Pichugin (HLAHP) mechanism of $\mathrm{I}_2$ dissociation, based on the analysis of [18], where pathways involving the excited species $\mathrm{I}_2(X^1\Sigma_g^+, 10 \le v < 25)$, $I_2(X^1\Sigma_g^+, 25 \le v \le 47)$, $\mathrm{I}_2(A'^3\Pi_{2u})$, $\mathrm{I}_2(A^3\Pi_{1u})$, $\mathrm{O}_2(X^3\Sigma_g^-, v)$, $\mathrm{O}_2(a^1\Delta_g, v)$, $\mathrm{O}_2(b^1\Sigma_g^+, v)$ and $\mathrm{I}(^2P_{1/2})$ as intermediate reactants are included. The HLAHP mechanism was applied to the supersonic COIL modeling in [8] and [9] and predicted both the gain and the power that fit the experimental values for different types of COIL over a wide range of parameters. Table 1 lists the reactions considered in the modeling and their rate constants.

Power computations were performed just as in [9]. The stimulated emission rate is given by

$$R_{\mathrm{stim}} = g_{\mathrm{s}}\frac{2\tilde{I}}{h\nu}, \tag{4}$$

where $g_{\mathrm{s}}$ is the saturated gain of the laser transition, i.e., the value of $g$ in Eq. (2) once the process of the stimulated emission is incorporated in the calculation of [I*] and [I], $\tilde{I}$ is the intracavity circulating intensity propagating in one direction, and $h\nu$ is the energy of an $\mathrm{I}^* \rightarrow \mathrm{I}$ photon. The term $R_{\mathrm{stim}}$ is included in the kinetic equations for the species I* and I solved in the optical resonator. Also, the energy equation has a source term, $-2g_{\mathrm{s}}\tilde{I}$, to account for the laser energy emitted from the resonator. Just as in the experimental setup, the optical axis of the resonator is transverse to the flow direction. The model of constant intracavity intensity $\tilde{I}$ described in [9] and [20] was used for the power computations. The fact that $\tilde{I}$ is independent of the distance in the optical axis direction follows from Rigrod's analysis [23] in the limiting case $g_{\mathrm{s}}L \ll 1$, where $L$ is the gain length. $\tilde{I}$ is found from the following condition:

$$g_{\mathrm{s,av}} = \frac{\int_V g_{\mathrm{s}}(x, y, z)\,dx\,dy\,dz}{V} = g_{\mathrm{th}}, \tag{5}$$

where $g_{\mathrm{s,av}}$ is the gain averaged over the resonator active volume, $V$, $g_{\mathrm{th}} \equiv (t + a)/2L$ is the threshold gain, and $t$ and $a$ are the total transmission and absorption/scattering/diffraction losses of the mirrors per round trip. An iterative method of trial and error was used to find the value of $\tilde{I}$ for which Eq. (5)) (where $g_{\mathrm{s}}$ strongly depends on $\tilde{I}$) holds and 10–15 iterations were needed for it. The power is given by $P = \tilde{I}St$, where $S$ is the output aperture cross section.

## 3 Comparison between 1D and 3D CFD models and experimental measurements

The input parameters of the model include the boundary conditions for the primary and secondary flow inlets (flow rates of the different species and the temperatures) and pressures measured in the subsonic section of the nozzle and at three different points downstream of the supersonic nozzle exit plane. The boundary conditions shown in Table 2 are the same as in [8] (gain runs 1–3) and [9] (lasing run) where 3D modeling of the gain and lasing power, respectively, was performed. The values of $g$, $F$ and $T$ were calculated for runs 1–3, whereas the output power was calculated in the lasing run. Measured pressures depend on the iodine flow rate; as a result, the number of the pressure values is too large to be presented in the paper. We only mention that typical values of the pressure in the subsonic section and resonator optical axis are 11 and 2 Torr, respectively.

Figures 2, 3 and 4 show the calculated (using 1D and 3D models) and experimental dependence of $g$, $F$, and $T$, respectively, on $n\mathrm{I}_2$ at the optical axis of the 5-mm throat profiled nozzle shown in Fig. 1(a). The calculated results, averaged for the three runs, are shown for the boundary conditions presented in Table 2. Just as in [6], the averaging was done since the experimental values of $g$, $F$, and $T$ measured at different runs for the same $n\mathrm{I}_2$ are very close to each other, the differences being smaller than the error bars indicated in

**Table 1** Reactions considered in the modeling (HLAHP scheme). $I_2^{\dagger}$ and $I_2^{\dagger\dagger}$ designate $I_2(10 \le v < 25)$ and $I_2(25 \le v \le 47)$, respectively, and $k_f$ and $k_b$ are forward and backward rate constants [8]

| No. | Reaction | Rate constant ($cm^3$ $molecule^{-1}$ $s^{-1}$) |
|---|---|---|
| 1 | $O_2(a) + I_2 \rightarrow O_2(X) + I_2^{\dagger\dagger}$ | 0 |
| 2′ | $I^* + I_2 \rightarrow I + I_2^{\dagger\dagger}$ | $3.8 \times 10^{-11}\Gamma$, $\Gamma = 0.25$ |
| 2″ | $I^* + I_2 \rightarrow I + I_2^{\dagger}$ | $3.8 \times 10^{-11}(1-\Gamma)$ |
| 3 | $O_2(a) + I \leftrightarrow O_2(X) + I^*$ | $k_f = 7.8 \times 10^{-11}$<br>$k_b = k_f/[0.75\exp(401.4/T)]$ |
| 4 | $O_2(a) + I_2^{\dagger\dagger} \rightarrow O_2(X) + 2I$ | $3.0 \times 10^{-10}$ |
| 5 | $O_2(a) + I_2^{\dagger} \rightarrow O_2(X) + I_2(A', A)$ | $2 \times 10^{-11}$ |
| 6 | $O_2(b) + I_2 \rightarrow O_2(X) + 2I$ | $3.5 \times 10^{-11}$ |
| 7 | $I^* + H_2O \rightarrow I + H_2O$ | $2.0 \times 10^{-12}$ |
| 8 | $I_2^{\dagger} + N_2 \rightarrow I_2 + N_2$ | $1.5 \times 10^{-12}$ |
| 9 | $I_2^{\dagger} + O_2 \rightarrow I_2 + O_2$ | $1.2 \times 10^{-12}$ |
| 10 | $O_2(b) + I_2 \rightarrow O_2(a) + I_2$ | $2.5 \times 10^{-11}$ |
| 11 | $O_2(a, v=1) + I_2 \rightarrow O_2(X) + I_2(A')$ | $1.9 \times 10^{-11}\exp(-897/T)$ |
| 12 | $O_2(a, v=2) + I_2 \rightarrow O_2(X) + I_2(A)$ | $3.0 \times 10^{-11}$ |
| 13 | $O_2(a, v=3) + I_2 \rightarrow O_2(X) + 2I$ | $1.0 \times 10^{-11}$ |
| 14 | $O_2(a) + I_2(A', A) \rightarrow O_2(X) + 2I$ | $3.0 \times 10^{-10}$ |
| 15 | $O_2(a) + O_2(a) \rightarrow O_2(b, v=2) + O_2(X)$ | $9.5 \times 10^{-28}T^{3.8}\exp(700/T)$ |
| 16 | $O_2(a) + O_2(a) \rightarrow 2O_2(X, v=3)$ | $1.7 \times 10^{-17}$ |
| 17 | $O_2(b) + H_2O \rightarrow O_2(a, v=3) + H_2O$ | $6.7 \times 10^{-12}$ |
| 18 | $O_2(a) + I^* \rightarrow O_2(b, v=2) + I$ | $4 \times 10^{-24}T^{3.8}\exp(700/T)$ |
| 19 | $O_2(a) + I^* \rightarrow O_2(a, v=3) + I$ | $1.1 \times 10^{-13}$ |
| 20 | $O_2(a, v=1) + O_2(X, v=0) \leftrightarrow O_2(X, v=1) + O_2(a, v=0)$ | $k_f = 7.9 \times 10^{-11}\exp(-104/T)$<br>$k_b = 7.9 \times 10^{-11}$ |
| 21 | $O_2(a, v=2) + O_2(X, v=0) \leftrightarrow O_2(X, v=2) + O_2(a, v=0)$ | $k_f = 7.3 \times 10^{-11} \times \exp(-213/T)$<br>$k_b = 7.3 \times 10^{-11}$ |
| 22 | $O_2(a, v=3) + O_2(X, v=0) \leftrightarrow O_2(X, v=3) + O_2(a, v=0)$ | $k_f = 7 \times 10^{-11}\exp(-327/T)$<br>$k_b = 7 \times 10^{-11}$ |
| 23 | $O_2(b, v=1) + O_2(X, v=0) \leftrightarrow O_2(X, v=1) + O_2(b, v=0)$ | $k_f = 2.51 \times 10^{-11}\exp(-151/T)$<br>$k_b = 2.51 \times 10^{-11}$ |
| 24 | $O_2(b, v=2) + O_2(X, v=0) \leftrightarrow O_2(X, v=2) + O_2(b, v=0)$ | $k_f = 4.73 \times 10^{-12}\exp(-307/T)$<br>$k_b = 4.73 \times 10^{-12}$ |
| 25 | $O_2(X, v=2) + O_2(X, v=0) \leftrightarrow 2O_2(X, v=1)$ | $k_f = k_b = 2 \times 10^{-13}$ |
| 26 | $O_2(X, v=3) + O_2(X, v=0) \leftrightarrow O_2(X, v=2) + O_2(X, v=1)$ | $k_f = k_b = 2.6 \times 10^{-13}$ |
| 27 | $O_2(a, v=1) + H_2O \leftrightarrow O_2(a, v=0) + H_2O$ | $k_f = 5.5 \times 10^{-13}$<br>$k_b = 5.5 \times 10^{-13}\exp(-2241/T)$ |
| 28 | $O_2(X, v=1) + H_2O \leftrightarrow O_2(X, v=0) + H_2O$ | $k_f = 5.5 \times 10^{-13}$<br>$k_b = 5.5 \times 10^{-13}\exp(-2138/T)$ |
| 29 | $I_2(A') + O_2(X) \rightarrow I_2 + O_2(a)$ | $6.3 \times 10^{-12}$ |
| 30 | $I_2(A) + O_2(X) \rightarrow I_2 + O_2(a)$ | $6.3 \times 10^{-12}$ |

Figs. 2, 3 and 4. The results calculated using the 3D model and experimental points are the same as in [8]. The values of $g$ and $F$ calculated using the 1D model are in good agreement with those calculated using the 3D model and with the measured values over the whole range of $nI_2$ except for low $nI_2 \le 0.25$ mmole/s where the 1D model predicts larger $F$ than in the 3D model. $T$ predicted by the 1D model is a little lower than that calculated by the 3D model but is closer to the measured values (Fig. 4).

It is worth noting that unlike the present model, that assumes instantaneous premixing of the primary and secondary flows (in the supersonic region), some of the previous models of the COIL ([10–13] and [21]), based on the old Heidner mechanism of $I_2$ dissociation [22], assumed grad-

ual mixing between the primary and secondary flows (in the subsonic region), starting at the exit of the $I_2$ injection holes located upstream of the throat. The last assumption enables increasing of the $I_2$ dissociation rate, which as shown in [6–8] was underestimated by Heidner's mechanism. Indeed, the initial local number density of the iodine injected into the oxygen flow and concentrated in very narrow jets downstream of the injection hole exit might be very high resulting in substantial acceleration of $I_2$ dissociation rate and achievement of substantial values of $F$ at the optical axis for Heidner's model. The present model uses the HLAHP mechanism for which the rate of $I_2$ dissociation is substantially larger than for Heidner's mechanism [8]; hence, as shown in Fig. 3, high values of $F$ (>0.5), close to those predicted by the 3D model and only a little smaller (within the error bar) than the experimental values, are achieved under the assumption of instantaneous mixing at the aerodynamic throat. Note that the reason for smaller $F$ is not related to the last assumption since the 3D model, where the mixing starts at the injection location, predicts almost the same values of $F$.

Figure 5 shows comparison between the values of the power $P$ calculated by 1D and 3D models at different $nI_2$ for the 8-mm throat nozzle shown in Fig. 1(b). The calculated results are shown for the boundary conditions of the lasing run presented in Table 2. Figure 5 shows also the values of $P$ measured for the same nozzle and flow conditions. Results calculated using the 3D model and the experimental points are the same as in [9]. The total mirror transmission $t$ and losses $a$ are 0.7 and 0.05 %, respectively. The error bars for the calculated results show the span of the power due to uncertainty in the yield (±0.03) and mirror losses $a$ (±0.05 %) [9], whereas the experimental error of the power measurement shown by the square markers is estimated to be ±5 W.

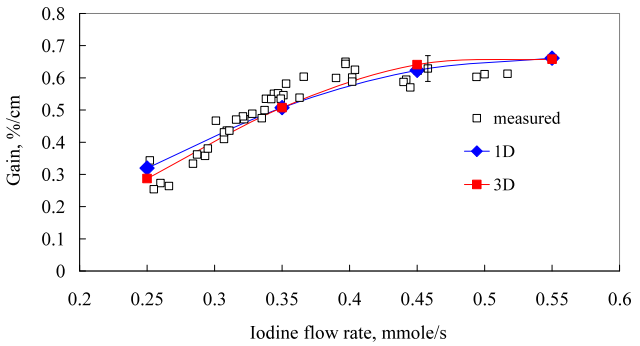


**Fig. 2** Measured and calculated (using 1D and 3D CFD HLAHP models) dependence of the gain on the iodine flow rate at the optical axis of the COIL described in [8]. The calculated gain is averaged over runs 1, 2 and 3 (Table 2)

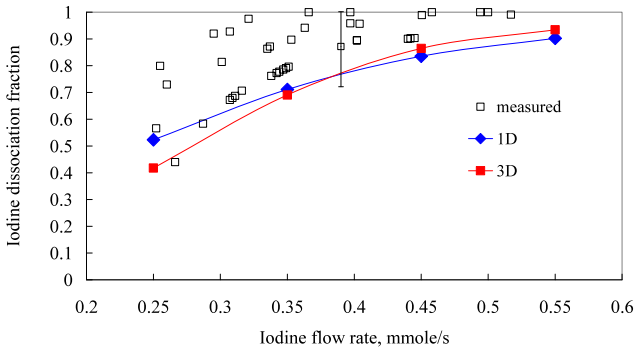


**Fig. 3** Measured and calculated (using 1D and 3D CFD HLAHP models) dependence of the $I_2$ dissociation fraction on the iodine flow rate at the optical axis of the low pressure COIL described in [8]. The calculated $I_2$ dissociation fraction is averaged over runs 1, 2 and 3 (Table 2)

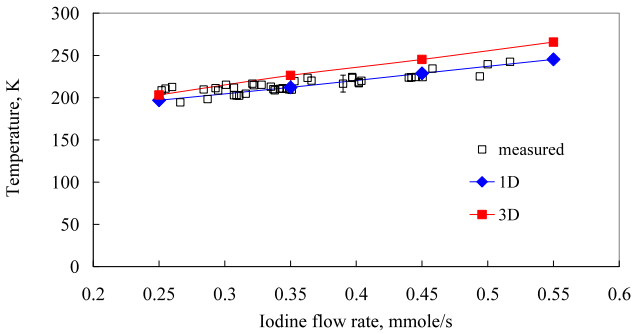


**Fig. 4** Measured and calculated (using 1D and 3D CFD HLAHP models) dependence of the temperature on the iodine flow rate at the optical axis of the low pressure COIL described in [8]. The calculated temperature is averaged over runs 1, 2 and 3 (Table 2)

**Table 2** Boundary conditions for the primary and secondary flows used in the calculations of $g$, $F$, $T$ and the output lasing power

| Initial temperature | Species and $O_2(a)$ yield | Flow rate (mmole/s) | | |
|---|---|---|---|---|
| | | Run 1 | Runs 2 and 3 | Lasing run |
| | | calculations of $g$, $F$ and $T$ | | calculations of $P$ |
| Primary flow, $T = 335$ K | $O_2$ | 16.15 | | 16.53 |
| | yield | 0.49 | 0.55 | 0.7 |
| | $Cl_2$ | 0.85 | | 0.87 |
| | $H_2O$ | 1.50 | 2.32 | 1.5 |
| Secondary flow, $T = 350$ K | $I_2(X)$ | 0.25–0.55 | | 0.3–0.5 |
| | $N_2$ | 28.00 | | |

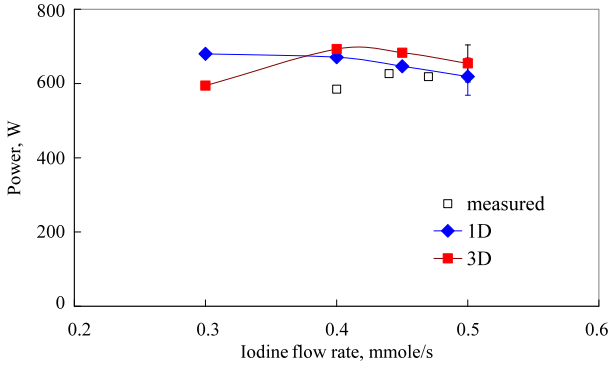


**Fig. 5** Measured and calculated (using 1D and 3D CFD HLAHP models) dependence of the lasing output power on the iodine flow rate in the COIL with the 8-mm throat non-profiled nozzle shown in Fig. 1(b) [9]. The boundary conditions for the flow are presented in Table 2 (lasing run), the mirror transmission $t$ and losses $a$ are 0.7 and 0.05 %, respectively. The error bars for the calculated results show the span of the power due to uncertainty in the yield (±0.03) and mirror losses $a$ (±0.05 %)

The values of $P$ calculated by the 1D model are in good agreement with those calculated using the 3D model for $nI_2 \geq 0.3$ mmole/s. Predictions of both models are in a satisfactory agreement with the measured values, the values of $P$ calculated by the 1D model being even closer to the experimental points than those predicted by 3D model.

## 4 Summary

The 1D model of the supersonic COIL is compared with the 3D models reported in [8] and [9] and the experimental measurements of the COIL parameters presented in [6, 9] and [16]. The present model is based on our previous 1D model of the supersonic COIL reported in [15], however there are several important differences between the models: (i) the present model is applied to the COIL where $I_2$ is injected in the supersonic section of the nozzle whereas the model reported in [15] treats the transonic injection of $I_2$; (ii) the present model employs the HLAHP mechanism for $I_2$ dissociation which, as shown in [8] and [9], describes the operation of the COIL much better than the Heidner mechanism [22] employed in our previous 1D model [15]; (iii) unlike the 1D model reported in [15], which calculated only the gain $g$, $I_2$ dissociation fraction $F$ and temperature $T$, the present model also calculates the output lasing power $P$.

The dependence of $g$, $F$, $T$ and $P$ on the iodine flow, calculated using the 1D model, is in good agreement with that found using 3D models and experimental results. Hence the 1D model can be used rather than the much more complicated 3D models for estimates of the working parameters of supersonic COILs. The main advantage of the 1D model over the 3D models is short computation time of less than 10 seconds per run. However, 1D models cannot predict some important features of the COIL such as the spatial flow pattern, gain and temperature distributions across the flow, output intensity spatial distribution in the laser spot and the influence of the boundary layers on the pressure distribution along the flow, which in our 1D model was taken from the experimental measurements (see Sect. 3). All these parameters can be calculated with the aid of 3D models which still remain very useful computational tools for the COIL despite the very long computation time, four orders of magnitude longer than for 1D models. In particular, the present 1D model, that assumes instantaneous premixing of the primary and secondary flows, is applicable only to COILs with nozzles and injectors providing fast mixing of the primary and secondary streams. On the other hand, for COILs with slow supersonic mixing of the parallel jets of oxygen and $I_2/N_2$ mixture [24], application of this model is questionable and 3D CFD model should be applied.

## Appendix: Conservation equations in the mixed stream

The equations for $\omega(Z)$ have the form:

$$\frac{d\omega(Z)}{dx} = m(Z) \cdot R(Z) \cdot A, \tag{6}$$

where $x$ is the distance along the flow, $m(Z)$ the molecular weight of the $Z$-component, $R(Z)$ the chemical production rate of species $Z$, and $A$ is the total cross section area of the mixed stream. Unlike [15], the terms corresponding to entrainment of the primary gas into the mixed layer were not included since, as mentioned in Sect. 2, for the entire mixing the primary stream was absent downstream of the instantaneous mixing in the aerodynamic throat.

The dependencies of $A$, $U$ and $T$ are found from the mass, momentum and energy conservation equations:

$$A = \frac{\omega \cdot k \cdot T}{p \cdot U \cdot m}, \tag{7}$$

$$\frac{d(\omega \cdot U)}{dx} = -A\frac{dp}{dx}, \tag{8}$$

$$\frac{d[\omega(h + c_p T + U^2/2)]}{dx} = 0, \tag{9}$$

where $\omega = \sum_Z \omega(Z)$, $m = \sum_Z \omega(Z) \cdot m(Z)/\omega$ is the average molecular mass, $h$ and $c_p$ are the specific (per unit mass) enthalpy and heat capacities, given by $h = \sum_Z \omega(Z) \cdot h(Z)/\omega$ and $c_p = \sum_Z \omega(Z) \cdot c_p(Z)/\omega$, respectively, and $h(Z)$ and $c_p(Z)$ are the specific enthalpy of formation and heat capacity for the $Z$-component.

## References

1. W.E. McDermott, N.R. Pchelkin, D.J. Benard, R.R. Bousek, Appl. Phys. Lett. **32**, 469 (1978)
2. M. Suzuki, T. Suzuki, W. Masuda, Proc. SPIE **4184**, 99 (2001)

3. T.G. Madden, Proc. SPIE **5120**, 363 (2003)
4. A.S. Boreisho, A.B. Barkan, D.N. Vasil'ev, I.M. Evdokimov, A.V. Savin, Quantum Electron. **35**, 495 (2005)
5. T. Madden, Proc. SPIE **6346**, 634620 (2007)
6. K. Waichman, V. Rybalkin, A. Katz, Z. Dahan, B.D. Barmashenko, S. Rosenwaks, J. Appl. Phys. **102**, 013108 (2007)
7. K. Waichman, B.D. Barmashenko, S. Rosenwaks, J. Appl. Phys. **104**, 013113 (2008)
8. K. Waichman, B.D. Barmashenko, S. Rosenwaks, J. Appl. Phys. **106**, 063108 (2009)
9. K. Waichman, B.D. Barmashenko, S. Rosenwaks, J. Chem. Phys. **133**, 084301 (2010)
10. B.D. Barmashenko, A. Elior, E. Lebiush, S. Rosenwaks, J. Appl. Phys. **75**, 7653 (1994)
11. A. Elior, B.D. Barmashenko, E. Lebiush, S. Rosenwaks, Appl. Phys. B **61**, 37 (1995)
12. D.L. Carroll, AIAA J. **33**, 1454 (1995)
13. B.D. Barmashenko, S. Rosenwaks, AIAA J. **34**, 2569 (1996)
14. T.T. Yang, R.A. Cover, V. Quan, D.M. Smith, A.H. Bauer, W.E. McDermott, D.A. Copeland, Proc. SPIE **2989**, 126 (1997)
15. E. Bruins, D. Furman, V. Rybalkin, B.D. Barmashenko, S. Rosenwaks, IEEE J. Quantum Electron. **38**, 345 (2002)
16. V. Rybalkin, A. Katz, B.D. Barmashenko, S. Rosenwaks, J. Appl. Phys. **98**, 023106 (2005)
17. V. Rybalkin, A. Katz, E. Bruins, D. Furman, B.D. Barmashenko, S. Rosenwaks, IEEE J. Quantum Electron. **38**, 1398 (2002)
18. V.N. Azyazov, S.Yu. Pichugin, M.C. Heaven, J. Chem. Phys. **130**, 104306 (2009)
19. M.V. Zagidullin, V.D. Nikolaev, M.I. Svistun, N.A. Khvatov, B.T. Anderson, R.F. Tate, G.D. Hager, Quantum Electron. **31**, 678 (2001)
20. B.D. Barmashenko, D. Furman, S. Rosenwaks, Appl. Opt. **37**, 5697 (1998)
21. J.A. Miller, E.J. Jumper, AIAA J. **32**, 1228 (1994)
22. R.F. Heidner III, C.E. Gardner, G.I. Segal, T.M. El-Sayed, J. Phys. Chem. **87**, 2348 (1983)
23. W. Rigrod, IEEE J. Quantum Electron. **14**, 377 (1978)
24. V.N. Azyazov, M.V. Zagidullin, V.N. Nikolaev, V.S. Safonov, Quantum Electron. **27**, 477 (1997)